

Article

A Novel Underwater Simultaneous Localization and Mapping Online Algorithm Based on Neural Network

Guangchao Hou ¹, Qi Shao ¹, Bo Zou ¹, Liwen Dai ², Zhe Zhang ³, Zhehan Mu ¹,
Yadong Zhang ⁴ and Jingsheng Zhai ^{1,*}

¹ School of Marine Science and Technology, Tianjin University, Tianjin 300072, China;
houguangchao@tju.edu.cn (G.H.); shaoqi@tju.edu.cn (Q.S.); zouboyou@tju.edu.cn (B.Z.);
muzhehan@tju.edu.cn (Z.M.)

² Taozhongling National Nature Reserve, Jiujiang 332700, China; liwendai@outlook.com

³ Tianjin Jinhang Institute of Technical Physics, Tianjin 300308, China; zhangzhe_tianjin@outlook.com

⁴ School of Architecture, Inner Mongolia University of Science and Technology, Baotou 014010, China;
zhangyadong_lu@outlook.com

* Correspondence: jingsheng@tju.edu.cn

Received: 5 November 2019; Accepted: 18 December 2019; Published: 19 December 2019



Abstract: The navigation and localization of autonomous underwater vehicles (AUVs) in seawater are of the utmost importance for scientific research, petroleum engineering, search and rescue, and military missions concerning the special environment of seawater. However, there is still no general method for AUVs navigation and localization, especially in the featureless seabed. The reported approaches to solving AUVs navigation and localization problems employ an expensive inertial navigation system (INS), with cumulative errors and dead reckoning, and a high-cost long baseline (LBL) in a featureless subsea. In this study, a simultaneous localization and mapping (AMB-SLAM) online algorithm, based on acoustic and magnetic beacons, was proposed. The AMB-SLAM online algorithm is based on multiple randomly distributed beacons of low-frequency magnetic fields and a single fixed acoustic beacon for location and mapping. The experimental results show that the performance of the AMB-SLAM online algorithm has a high robustness. The proposed approach (the AMB-SLAM online algorithm) provides a low-complexity, low-cost, and high-precision online solution to the AUVs navigation and localization problem in featureless seawater environments. The AMB-SLAM online solution could enable AUVs to autonomously explore or autonomously intervene in featureless seawater environments, which would enable AUVs to accomplish fully autonomous survey missions.

Keywords: AUVs; AMB-SLAM; neural network; magnetic beacons

1. Introduction

Autonomous underwater vehicles (AUVs) play a crucial role in many subsea missions and are widely used in scientific research, search and rescue, the military, petroleum engineering, and civilian applications [1,2]. To execute these missions, precise navigation and localization are the most important technologies for pursuing a preprogrammed trajectory and acquiring accurate geographic data. Generally speaking, above water, most unmanned aerial vehicles (UAVs) and unmanned surface vessels (USVs) are remotely operated by radio and navigated by an inertial navigation system (INS) or global positioning system (GPS) [3]. Nevertheless, under the sea, GPS and radio signals are unavailable, because electromagnetic radiation cannot adequately penetrate the unstructured nature of the undersea environment. Furthermore, underwater communication is highly restricted by the environmental factors of seawater, such as the temperature, pressure, or salinity of the seawater. While there are

so many significant challenges, AUV navigation and localization technologies have grown in leaps and bounds over more than half a century due to the need to remarkably expand the capabilities of AUVs. AUVs have been widely used in many underwater fields, especially petroleum engineering [4], underwater built environments, marine science research [5], and search and rescue [6–8].

In comparison with electromagnetic navigation technology, underwater acoustic-based sensors work better in seawater [1]. Therefore, acoustic-based navigation technologies are widely used in underwater vehicle positioning. In these acoustic navigation technologies, including the long baseline (LBL), ultra-short baseline (USBL), and short baseline (SLB) technologies, localization is accomplished by computing the relative position from the time of flight (TOF) of acoustic signals [9]. Compared with SBL and USBL, LBL has a perfect geometry in positioning, which allows for a greater navigation accuracy. Thus, LBL systems are generally applied in tasks that require a higher position precision, especially in high-risk situations, such as under-ice surveys [10,11] and deep-water surveys [12]. Nevertheless, in most cases, it is essential that acoustic transponders are deployed and globally georeferenced by a surface ship [13], a helicopter [10], GPS [9], or even another AUV [14], prior to conducting missions, and they need to be retrieved after the task is complete.

The deployment, georeferencing, and recovery of each deployed transponder from the seafloor adds significant time and cost to any AUV mission. To overcome these problems, LaPointe [15] proposed a virtual LBL (VLBL) method, which localizes AUVs using only one fixed transponder. Unlike the LBL method, in [16–20], an extended underwater GPS navigation technology was proposed, called the GPS intelligent buoy (GIB) system, which involves inverted LBL devices, where the submarine acoustic array is replaced by floating surface buoys equipped with GPS receptors that emit satellite navigation information underwater by an acoustic signal.

Nevertheless, none of the acoustic navigation techniques constitutes a faultless solution to the challenge of AUVs navigation. Batista et al. [21–23] proposed a novel acoustic navigation system based on the integration of the LBL and USBL systems, which could ensure high-precision positioning, irrespective of the depth. Vickery [24] proposed an integrated LBL/SBL/USBL positioning system, which has a more accurate positioning capacity than single conventional acoustic navigation on account of the observation redundancy. The acoustic navigation system, over longer ranges, typically offers a poor precision and low update rates. To circumvent that problem, Whitcomb et al. [25] and Spindel et al. [26] proposed a navigation method based on the combination of the LBL and Doppler velocity log (DVL) systems, which offers a remarkable improvement in terms of the vehicle navigation precision and update rate. However, the above solutions limit the operating area of AUVs.

While an AUV performs a scientific expedition at depths exceeding a certain depth, or it securely and stealthily navigates in military applications, INS is the only technology available, as a result of its precise location performance, which is independent of external sources [27]. However, the fatal drawback of INS is that it drifts over time, and even the best INS can only achieve a drift of 0.1% of the distance traveled [28]. Therefore, the integration of the other navigation methods and the INS, which allows them to complement each other, has been studied in order to improve the AUVs' performance in long-term missions. For example, in [29–32], a USBL and INS integration technology was presented to improve the navigation performance of AUVs. Choi et al. [33] and Knight [34] presented an underwater navigation method based on the fusion of the GPS and INS sensors. However, this method requires the AUV to surface for position correction. In order to alleviate the problem of DVL when it fails to maintain a bottom lock, Tal et al. [35] proposed a navigation system based on INS, aided by a DVL, magnetometer, and pressure sensor (PS).

While acoustic navigation, INS navigation, and the combination of two or more methods could provide a bounded navigation error, this would enhance the cost of AUV missions and the complexity of data fusion. A novel technology, simultaneous localization and mapping (SLAM), has been proposed to allow indoor and outdoor robots to precisely navigate without the use of auxiliary equipment [36,37]. It is possible for the SLAM technique to incrementally build a features map that is consistent with its unknown surroundings and simultaneously determine its location within this

map [38]. At present, SLAM is an extremely mature technology in the navigation and positioning of unmanned ground vehicles (UGVs) [39] and unmanned aerial vehicles (UAVs) [40,41]. Nevertheless, the underwater communication technology and some important technical links of SLAM restrict the application of the SLAM technology in the underwater environment. In recent years, thanks to the rapid development of underwater communication technology, especially underwater modem technology, and the advancement in underwater SLAM research, SLAM has been applied in underwater localization and navigation [42,43].

In general, underwater SLAM utilizes geophysical information on the external environment around underwater vehicles for localization. According to the different ways of extracting the features of the external environment, underwater SLAM can be divided into sonar SLAM [44], optical SLAM [12,45,46], and magnetic SLAM.

Sonar SLAM acoustically acquires geophysical features by acoustic sonar, and then identifies and classifies features in the underwater environment that could be used as navigation landmarks. In general, sonar SLAM could fall into one of two main categories: ranging sonar SLAM and imaging sonar SLAM, according to the sonar types. Ranging sonar SLAM usually obtains geophysical data by an echo sounder [47,48], sub-bottom profile [49] and multi-beam echo sounder (MBES) [50–54]. The quality of the navigation of the ranging sonar SLAM depends on its transducer quality, operating frequency, and altitude from the seafloor. For the imaging sonar SLAM, the type of sonar used includes a side-scan sonar (SSS) [55–58], forward-look sonar (FLS) [59], synthetic aperture sonar (SAS) [60,61], and mechanical scanned imaging sonar (MSIS) [62–64]. Unlike the ranging sonar SLAM, which yields 2.5-D bathymetric features (bathymetry elevation map), the image sonar SLAM produces a 2D imagery, and the performance of the former is much better than that of the latter [28,51].

In general, the optical SLAM utilizes a monocular or stereo camera to capture images of the seabed and then match these images for navigation [65]. The biggest drawback of optical SLAM is the reduced range of the cameras, susceptibility to scattering, and inadequate lighting [66,67]. In addition, the visual odometry and feature extraction relies on the existence of features. Therefore, optical underwater navigation methods are particularly well suited to the small-scale mapping of feature-rich environments [1,68]. Similar to sonar SLAM, the higher the quality of the navigation algorithm, the higher the quality of the data. While the use of magnetic field maps for localization has been proposed, no recent publications have been found [1].

However, both optical SLAM and sonar SLAM have fatal shortcomings. Firstly, the performance of the underwater SLAM algorithm is dependent on the number and quality of the features present in the environment. Secondly, the extraction of available features and matching them with the flat seafloor, which have little available features, are more challenging [69]. Finally, in general, underwater SLAM locates AUVs within its feature map only when the AUVs have finished their underwater operation missions. Then, another AUV mission can be scheduled to explore potential targets in the area of the first mission. Therefore, this solution significantly increases the time and the cost of the AUVs tasks.

In this study, we present an AMB-SLAM online navigation algorithm based on artificial neural network (ANN), which is based on the utilization of measurements made from the randomly distributed beacons of low-frequency magnetic fields, in addition to a single fixed acoustic beacon, on the featureless seafloor. The simulation experiments reported in this study demonstrate that using an unsophisticated low-cost magnetic beacons setup, it is possible to obtain geometrically consistent feature maps and an accurate trajectory for AUVs underwater navigation. In addition, in the present study, we compared the positioning accuracy of the AMB-SLAM online method and the magnetic-beacon-based SLAM (MB-SLAM) method, which only uses the information from magnetic beacons. The root mean square error (RMSE) of the AMB-SLAM online method is no more than 6 m, while the RMSE of the MB-SLAM is more than 15 m. The experimental results showed that the positioning accuracy of the AMB-SLAM online solution is significantly higher than that of the MB-SLAM, and the AMB-SLAM can achieve rapid and accurate positioning in underwater environments without features.

The remainder of the paper is organized as follows. Section 2 introduces the theoretical framework concerning the positioning principle of the magnetic beacon, artificial neural network (ANN), and the AMB-SLAM online algorithm. In Section 3, the simulation experiment is described in detail, and the results of applying the AMB-SLAM algorithm and a performance comparison with the MB-SLAM algorithm are presented. Finally, in Section 4, we discuss the AMB-SLAM method and summarize our major findings, provide a conclusion of the whole work, and give suggestions for future research.

2. Materials and Methods

2.1. Description of the Positioning Principle of the Beacon of the Low-Frequency Magnetic Field

As mentioned in the previous section, in the field of modern underwater navigation, no positioning method is a perfect solution on account of the particularity of the seawater environment. In simultaneous localization and mapping (SLAM) research, no one utilized magnetic field information as geophysical information for underwater localization. Davis [70] once measured the magnetic field intensity of the target point and then calculated the relative position between the target point and the magnetic beacon by taking advantage of the GPS positioning principle and the penetrability of the magnetic near field. However, in his research, only a theoretical formula is given, which is not feasible in practical experiments.

The method of magnetic field localization based on the fundamental principle of the Biot–Savart law is to use the low-frequency alternating magnetic field as the signal source. The Biot–Savart law explains the magnetic field produced by a current carrying segment. As shown in the Figure 1, a wire carries a specific direction current I , taking a small element of the wire of length d . The direction of this element is along that of the current so that it forms a vector \vec{Idl} . The magnitude of the magnetic field \vec{dB} at a distance r from a current carrying element dl is found to be proportional to I and to the length dl and is inversely proportional to the cubic of the distance r . The Biot–Savart law is formulated as follows:

$$\vec{dB} = \frac{\mu_0}{4\pi} \frac{\vec{Idl} \times \vec{r}}{r^3} \quad (1)$$

$$\vec{B} = \int_L \frac{\mu_0}{4\pi} \frac{\vec{Idl} \times \vec{r}}{r^3} \quad (2)$$

where \vec{dB} is the magnetic field at field point P , which is produced due to the current element \vec{Idl} ; \vec{dl} is the infinitesimal length of the conductor carrying the electric current I ; \vec{r} is the distance vector that specifies the direction of the distance r from the current element to the field point; L is the integration path; and μ_0 is the permeability of the vacuum, whose value is equal to $4\pi \times 10^{-7}$ Tm/A. r is defined as follows:

$$r = \sqrt{x^2 + y^2 + z^2} \quad (3)$$

where x , y and z are the positions of the field point in local coordinates. The position of the magnetic field source is considered to be (0 m, 0 m, 0 m).

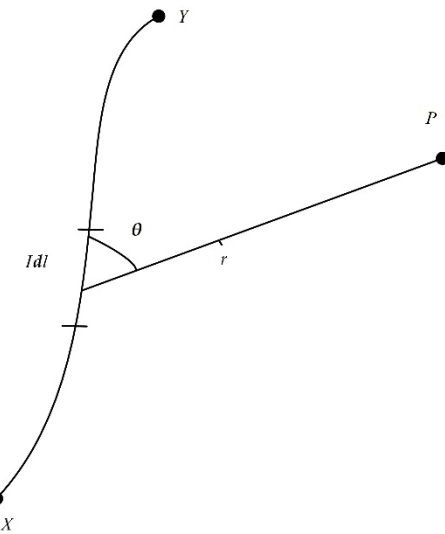


Figure 1. Biot–Savart law.

The Biot–Savart law is also true for superimposed magnetic fields. According to Formulas (1) and (2), if we know the magnitude of the magnetic field B and the current element $Id\vec{l}$, we can get the value of r , but we cannot measure the magnitude of the current element $Id\vec{l}$, so it is impossible to solve r by the Biot–Savart law in the experiment. Therefore, in the present study, we use the artificial neural network (ANN) to solve r .

2.2. Description of the Artificial Neural Network

The artificial neural network (ANN) can solve the optimization problem of the super nonlinear equation. Therefore, we use ANN to solve the nonlinear problem of magnetic field positioning. It simulates the human brain and nervous system from the perspective of information processing, establishes a mathematical model, and consists of a large number of complex interconnected neurons. Each neuron represents a specific output function, which is called an activation function. Each connection between two neurons represents a weighted value, which is equivalent to the memory of the artificial neural network. Learning in the human brain requires adjustments to the synaptic relationship between and among neurons, which is similar to the learning in ANN [71]. In order to circumvent the complicated nonlinear problem, multi-layer perceptrons (MLP), which are feed-forward neural networks, were proposed [71]. Thus, in this study, three hidden layers of MLP, in combination with the supervised learning method, called the error back propagation (BP) algorithm, were applied. The architecture of the selected MLP ANN is shown in Figure 2.

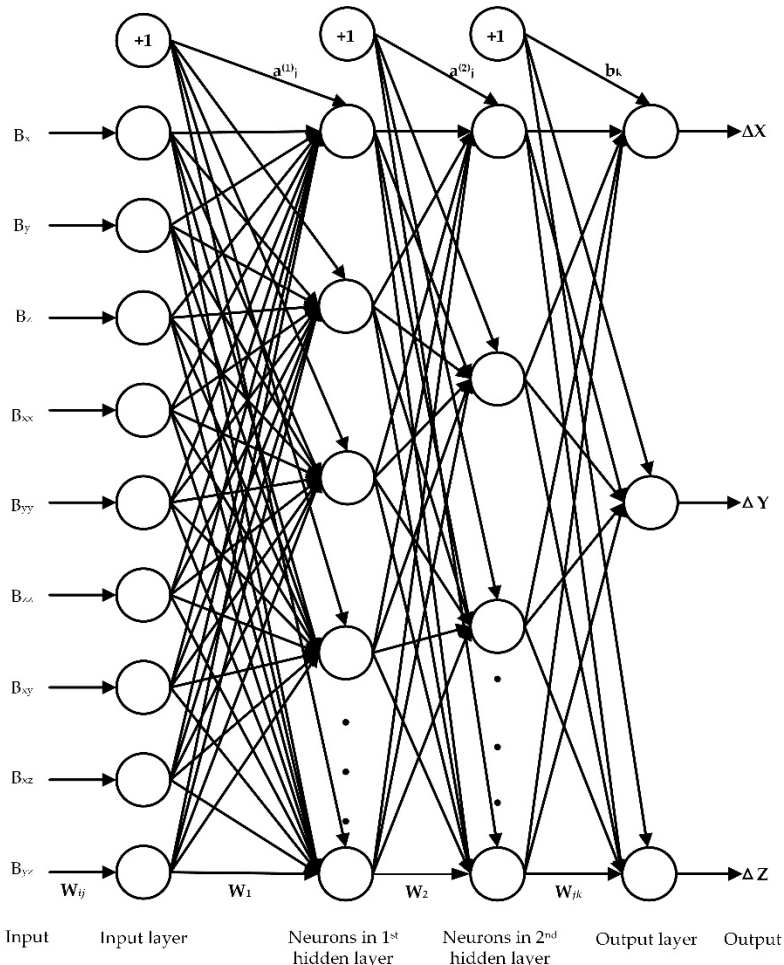


Figure 2. Schematic diagram of the proposed multi-layer perceptrons artificial neural network (MLP-ANN) model.

In the present study, it is assumed that the number of input layer neurons is n , the number of hidden layer neurons is l , and the number of output layer neurons is m . The forward propagation of MLP ANN is mainly composed of three parts. Firstly, MLP computes a linear weighted sum of its n inputs mathematically:

$$x_j = \sum_{i=1}^n w_{ij}x_i + a_j \quad (4)$$

where x_j is the linear weighted sum of all inputs, w_{ij} is the synapse weight between the i th neuron and j th neuron, x_i is the input vector, a_j is the bias value from the input layer to the hidden layer, and the subscript n denotes the number of input layer neurons. Then, the output of the hidden layer neurons can be represented as:

$$H_j = f(x_j) = f\left(\sum_{i=1}^n w_{ij}x_i + a_j\right) \quad (5)$$

where H_j is the output of hidden layer neurons, and $f(\cdot)$ is the activation function (see Formula (6)). In the present study, the chosen activation function is a hyperbolic tangent activation function:

$$f(x_j) = \frac{2}{1 + e^{(-2x_j)}} - 1. \quad (6)$$

Finally, the output of the output layer neuron of MLP-ANN can be represented as:

$$O_k = \sum_{j=1}^l H_j w_{jk} + b_j = \sum_{j=1}^l f\left(\sum_{i=1}^n w_{ij} x_i + a_j\right) w_{jk} + b_j \quad (7)$$

where w_{jk} is the connection weight between the j th neuron and the k th neuron, b_j is the bias value from the hidden layer to output layer, and the subscript l denotes the number of hidden layer neurons.

2.3. Optimization of MLP-ANN

In the present study, MLP-ANN is optimized by the unsupervised optimization method (or learning method), which is called the error backward propagation (BP) algorithm. In the backward propagation of MLP-ANN, three processes are required: data preprocessing, training data, and validating data.

2.3.1. Data Preprocessing

In the present study, a feed-forward neural network (see Figure 2), with the supervised learning method, called the error back-propagation (BP) algorithm, was used for learning. In our work, we chose the hyperbolic tangent activation function as the activation function.

The magnetic field data and relative position between the magnetic beacons and AUV of the magnetic beacon, which were collected in the field, were taken as the sample data of the neural network. When limited sample data are available, it might be difficult to maximize the utilization of the representative input data set. Meanwhile, it is also essential that the training data and validation data are representative of the same population. Therefore, we adopted the holdout method [72,73], splitting the input data set into two subsets: 10% of the data for validation and the remaining data for training the network. In addition, different variables span different ranges, and not all sample data could receive the same attention during the training steps (see below). Thus, in this experiment, it is essential to scale all the sample data within a specified range using Equation (8). In addition, the scaling of the input sets must be compatible with the boundary of the activation function used in the output layer or hidden layer [74]. The standardization formula is defined as follows:

$$x_i = (f_{\max} - f_{\min}) \frac{x_i - x_{\min}}{x_{\max} - x_{\min}} + f_{\min} \quad (8)$$

where x_{\min} and x_{\max} are the minimum and maximum value of the input sets, respectively, f_{\min} and f_{\max} are the minimum and maximum value of the activation function, respectively, and the subscript i denotes the input data number. The value of the hyperbolic tangent transfer function is between -1 and 1 , therefore, the sample data are scaled within the range of -0.9 to 0.9 . Thus, Equation (8) is given as:

$$x_i = 1.8 \frac{x_i - x_{\min}}{x_{\max} - x_{\min}} - 0.9. \quad (9)$$

2.3.2. Training

After the preparation of the sample data set, the magnitude of the magnetic field B was set as the input and the relative position of the magnetic beacon and AUV r were set as the outputs.

The training process of ANN involves optimizing the neural weights by adjusting the internal parameters of MLP-ANN (such as the number of hidden layers, their neurons, and so on, as shown in Figure 3) by trial and error, which is also called ‘learning’. The purpose of learning is to find an optimal global solution for the highly nonlinear objective equation [75] and minimize the value of the error function. In the present study, the mean squared error (MSE) over the training samples was the

error function of the ANN performance evaluation to be optimized, and the minimization of the error function is performed by iterative techniques. The performance function is as follows:

$$E = \frac{1}{m} \sum_{k=1}^m (Y_k - O_k)^2 = \frac{1}{m} \sum_{k=1}^m e_k^2 \quad (10)$$

where Y_k represents the actual output, O_k represents the actual outputs, m denotes the number of output nodes, and e_k is the m th output residual. In order to attain the optimum architecture, different steps have been followed, according to the work flow diagram shown in Figure 3. The weight was optimized by the gradient-descent method. At the beginning of the training, the weights were initialized to zero-mean random values. This weight update equation is drawn from [76]:

$$w_{j+1} = w_j + \eta_j d_j \quad (11)$$

where w_{j+1} denotes the updated weights value, w_j denotes the initial weights value, η_j is the learning rate (η_j is proportional to the size of the steps), d_j is the direction of the descent, and the subscript n denotes the update time. The direction of descent d_j is the negative of the error gradient. The final weight update formula is

$$w_{j+1} = w_j - \eta_j \nabla_{w_j} E \quad (12)$$

where $\nabla_{w_j} E$ is the error gradient.

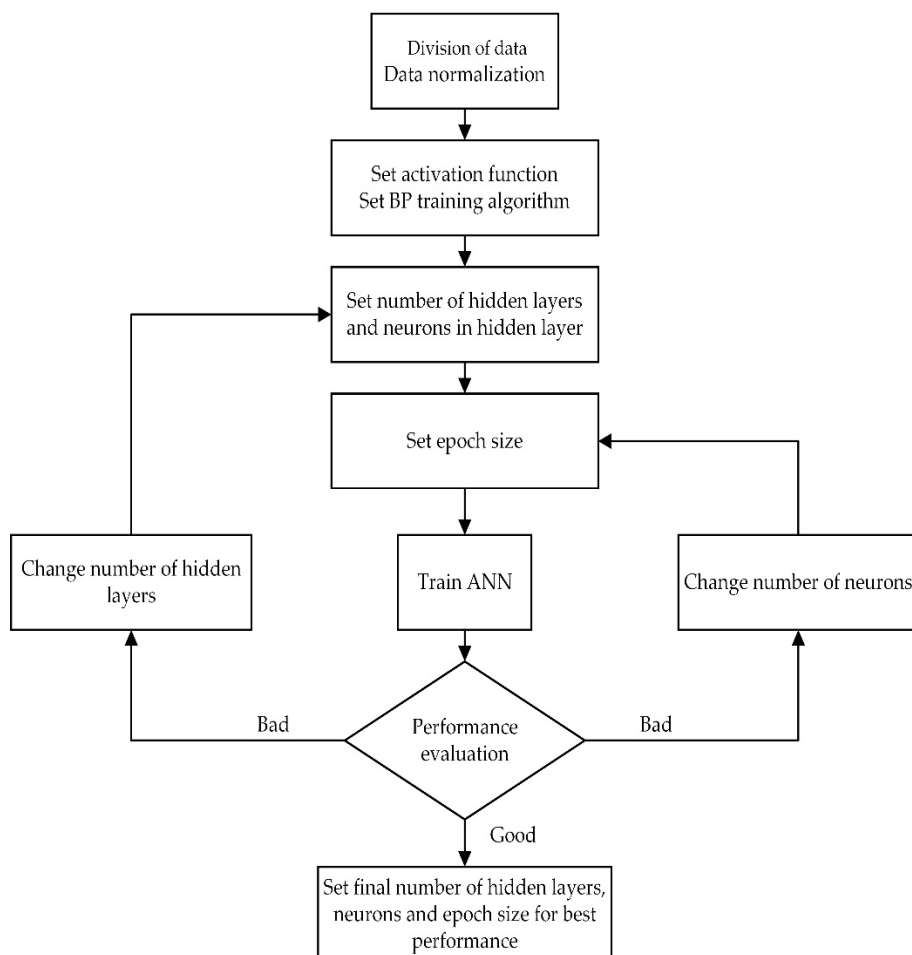


Figure 3. MLP-ANN training process for the best performance.

The architecture of MLP-ANN determines the number of connection weights and the number of hidden layers and neurons in each hidden layer. These hyper-parameters are normally determined through a trial and error method by comparison with the performance of different types of MLP-ANN architecture, as shown in the training flow in Figure 3. In addition, in order to prevent overfitting, the number of training samples is at least 30 times the number of connection weights [77] in this study. Similarly, the effect of the number of epochs on the performance of ANN was equally important. In this study, the number of epochs was set as the number of training samples [78]. Finally, the best MLP-ANN network is selected based on statistical criteria (MSE).

2.4. Description of the Proposed AMB-SLAM Algorithm

In this section, we will explain how the AMB-SLAM algorithm can map and locate AUVs in underwater environments without features. Figure 4 provides a basic schematic diagram of the AMB-SLAM algorithm. Before the AUV performs its mission, we randomly deploy a sufficient number of beacons of a low-frequency magnetic field to the area of interest. When the AUV observes the magnetic flux density of the No. 1, No. 2, and No. 3 magnetic beacon, it takes these values as the input values of the optimal MLP-ANN model to get the relative position Δx , Δy , Δz (see Figure 5) between these magnetic beacons and the AUV. The angle between the beacon and AUV are also available. In addition, the fixed acoustic beacon can constrain the AUV position in real time. If the absolute position of the acoustic beacon is known in the global coordinate system, we can obtain the position of the AUV through the coordinate conversion. The detailed flow chart of the AMB-SLAM algorithm, based on the extended Kalman filter (EKF), is shown in Figure 5.

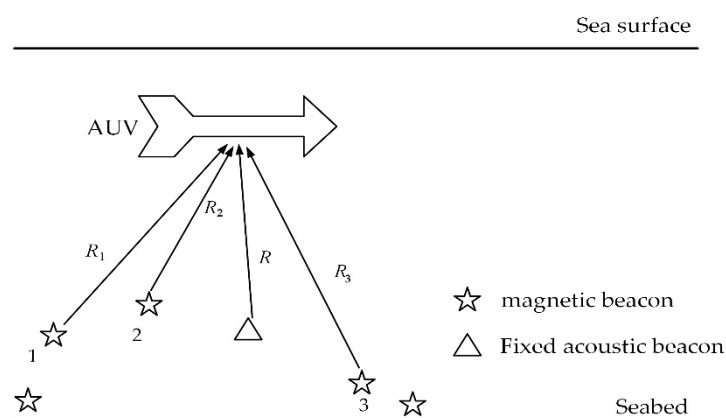


Figure 4. Schematic diagram of the AMB-SLAM algorithm.

When the AUV is in an unknown underwater environment, it conducts incremental environment modeling using the available geophysical information, which is gathered by an acoustic or optical sensor, and it uses the environment map to estimate its position. In this study, we assume that the initial position of the vehicle is (0 m, 0 m, 0 m), the relative position between the magnetic beacon and AUV can be estimated using the information from the observed magnetic beacons, and the position of the AUV can be updated by reobserving the beacons. The overall procedures of the AMB-SLAM, based the EKF filter navigation algorithm, are illustrated in Figure 5.

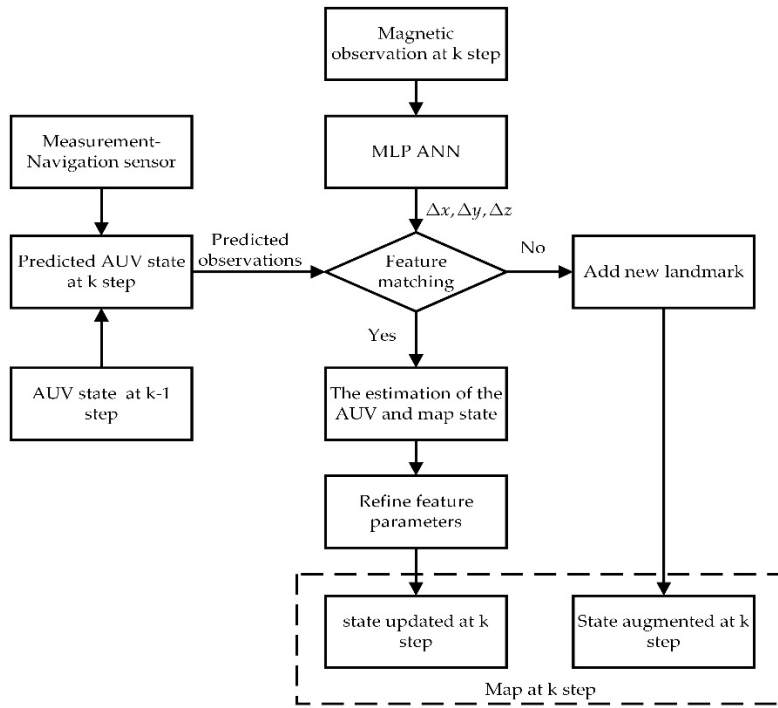


Figure 5. The flow chart of the simultaneous localization and mapping (AMB-SLAM) procedure based on the extended Kalman filter (EKF).

Now, supposing that these magnetic beacons are static landmarks with zero-input disturbance, the model of the i th beacon can be simplified as follows:

$$b_i^n(k) = b_i^n(k-1) \quad (13)$$

where $b_i^n(k)$ is the location of the i th beacon at time k .

As soon as the online feature extraction and the data association are in place, the AMB-SLAM algorithm includes the following three steps. Firstly, the AUV current state is predicted using the output values of MLP ANN. Secondly, the estimated state is updated from the reobserved landmark positions. Finally, the landmark map is updated.

2.4.1. State Equation

When the kinematics model of the AUV is known, the relative position of the magnetic beacon from the vehicle can be obtained through the optimal MLP-ANN model, and the augmented mathematical model of the state estimation can be established. The state is estimated using the EKF filter, and the AUV state is described by its local coordinates and heading angle as

$$X_v(k) = \begin{bmatrix} p_v(k) & \phi_v(k) \end{bmatrix}^T \quad (14)$$

with its covariance P_v

$$P_v = \begin{bmatrix} \sigma_{x_v x_v}^2 & \sigma_{x_v y_v}^2 & \sigma_{x_v \phi_v}^2 \\ \sigma_{x_v y_v}^2 & \sigma_{y_v y_v}^2 & \sigma_{y_v \phi_v}^2 \\ \sigma_{x_v \phi_v}^2 & \sigma_{y_v \phi_v}^2 & \sigma_{\phi_v \phi_v}^2 \end{bmatrix} \quad (15)$$

where $X_v(k)$ is the motion state of the AUV at time k , $p_v(k) = [x_v(k) \ y_v(k)]$ represents the position of the AUV in the local coordinate system, and $\phi_v(k)$ represents the AUV's heading angle at time k .

The coordinate of the n th feature is denoted as $\mathbf{x}_m(k) = (x_b(k), y_b(k))^T$, and the environmental landmarks can be denoted as

$$\mathbf{X}_m(k) = [x_b(1), y_b(1) \cdots, x_b(k), y_b(k)]^T \quad (16)$$

and its covariance matrix P_m is

$$P_m = \begin{bmatrix} \sigma_{x_1 x_1}^2 & \sigma_{x_1 y_1}^2 & \cdots & \sigma_{x_1 x_k}^2 & \sigma_{x_1 y_k}^2 \\ \sigma_{x_1 y_1}^2 & \sigma_{y_1 y_1}^2 & \cdots & \sigma_{y_1 x_k}^2 & \sigma_{y_1 y_k}^2 \\ \vdots & \vdots & \vdots & \vdots & \vdots \\ \sigma_{x_1 x_k}^2 & \sigma_{y_1 x_k}^2 & \cdots & \sigma_{x_k x_k}^2 & \sigma_{x_k y_k}^2 \\ \sigma_{x_1 y_k}^2 & \sigma_{y_1 y_k}^2 & \cdots & \sigma_{x_k y_k}^2 & \sigma_{y_k y_k}^2 \end{bmatrix} \quad (17)$$

The non-diagonal elements of the covariance matrix P_m are the cross-correlation information between different landmarks. We assume that the landmarks are stationary, and that their positions do not change over time. These correlations will be enhanced with each reobservation. The landmark map is represented by an augmented state vector:

$$\mathbf{X}_a(k) = [X_v(k) \quad \mathbf{X}_m(k)]^T. \quad (18)$$

If the change value of the AUV state is represented by the course change at the adjacent time, the distance change in the course direction and the vertical course direction can be written as $\Delta \mathbf{X} = [\Delta x \quad \Delta y \quad \Delta \phi]^T$, and the position of the AUV can be described as:

$$\begin{aligned} \mathbf{X}(k) &= \begin{bmatrix} x_v(k) \\ x_b(k) \end{bmatrix} \\ &= \begin{bmatrix} x(k) & y(k) & \phi(k) & x_b(k) \end{bmatrix}^T \\ &= \begin{bmatrix} x(k-1) + \Delta x \cdot \cos(\phi(k-1)) \\ y(k-1) + \Delta x \cdot \sin(\phi(k-1)) \\ \phi(k-1) + \Delta \phi \\ x_b(k-1) \end{bmatrix} \end{aligned} \quad (19)$$

According to the above state equation, the Jacobian matrix is represented as follows:

$$F = \begin{bmatrix} 1 & 0 & -\Delta x \cdot \sin(\phi(k-1)) & 0 \\ 0 & 1 & \Delta y \cdot \cos(\phi(k-1)) & 0 \\ 0 & 0 & 1 & 0 \\ 0 & 0 & 0 & I \end{bmatrix}. \quad (20)$$

2.4.2. Observation Equation

In the present study, the observation value is the relative position and the angle between the magnetic beacon and AUV. If an existing characteristic of the observed quantity and a state variable is determined, (x_{b_i}, y_{b_i}) is the position of the magnetic beacon in the map. Then, according to the estimated position of the AUV and the beacon b_i , we can get the estimated observation equation:

$$\hat{\mathbf{Z}} = h(\mathbf{X}(k)) = \begin{bmatrix} \sqrt{(x_{b_i} - x(k))^2 + (y_{b_i} - y(k))^2} \\ \arctan\left(\frac{y_{b_i} - y(k)}{x_{b_i} - x(k)}\right) - \phi(k) \end{bmatrix}. \quad (21)$$

In addition, we deploy an acoustic beacon on the seafloor. Thus, the AUV observes the distance and angle between the AUV and the fixed acoustic beacon, which is a constraint when the AUV

searches for the features, especially when there is no feature in the underwater, and it is the only useful information. To some extent, the positioning accuracy can be improved in this way.

The Jacobian matrix was obtained for the above observation equation:

$$H = \begin{bmatrix} \frac{x(k)-x_{b_i}}{r} & \frac{y(k)-y_{b_i}}{r} & 0 & \frac{x(k)-x_{b_i}}{r} & \frac{y(k)-y_{b_i}}{r} \\ \frac{y(k)-y_{b_i}}{r^2} & \frac{x(k)-x_{b_i}}{r^2} & -1 & \frac{y(k)-y_{b_i}}{r^2} & \frac{x(k)-x_{b_i}}{r^2} \end{bmatrix} \quad (22)$$

where r represents the distance between the beacon and AUV, and $r^2 = [x_{b_i} - x(k)]^2 + [y_{b_i} - y(k)]^2$.

Therefore, the problem of the position of the random magnetic beacon can be transformed into the problem of the standard nonlinear filtering problem. Since the Jacobian matrix of the state equation and the measurement equation have been obtained, the extended Kalman filter can be directly performed.

We define R to be the measurement covariance, and innovation v represents the difference between the true value and the predicted value:

$$v = z - \hat{z}. \quad (23)$$

The covariance matrix of the increment is

$$S = HP^{-1}H^T + R. \quad (24)$$

The Kalman gain W is expressed as

$$W = P^{-1}H^TS^{-1}. \quad (25)$$

The updated location and covariance can be described as

$$\hat{X}^* = \hat{X}^- + Wv \quad (26)$$

$$P^* = P^- + WSW^T. \quad (27)$$

Through the above formula, the neural network library and observation can be used to complete the synchronous update process of the vehicle and characteristic state. If no new features are observed, it can complete the iterative recursive process of prediction and updating in the next moment.

2.4.3. Updating

In the movement process of the AUV, it continuously explores new environments and discovers new beacons, so after completing the existing beacon position update, it needs to enlarge the dimensional state variables, add new beacons to the state vector, establish a craft condition, and map the relationship between the existing and new characteristics in order to construct an accurate map by merging these features.

Assuming that the sure measure $z = [r \ \phi]^T$ original from a new feature, (x, y) represents the position of the AUV, and r, ϕ represent the relative position and angle between the AUV and the new beacon, so the new beacon can be described as

$$X_b = u(X, z) = \begin{bmatrix} x + r \cos(\phi + \varphi_0) \\ y + r \sin(\phi + \varphi_0) \end{bmatrix}. \quad (28)$$

The new state is

$$X_a = [X \ X_b]^T \quad (29)$$

By adding new beacons, the algorithm realizes a step-by-step automatic map extension.

3. Experimental Results and Discussion

3.1. Data Sets

In order to train the MLP-ANN model for the best performance, one set of sample data was acquired in the waters of Weihai city, China (as shown in the Figure 6). The size of the field acquisition area is a square, with a side length of 500 m, and its water depth ranges from 14.6 m to 15.4 m. In our experiment, the beacons of a low-frequency magnetic field are composed of two orthodox solenoids (see Figure 7a), and the model of the triaxial magnetic component magnetometer model is MS3A-02 (see Figure 7b), with a measurement range of $-100 \mu\text{T} \sim 100 \mu\text{T}$ and measurement accuracy of 0.2 nT. In this experiment, the AUV maintains a speed of 5 m per second and is about 6 m above the seafloor.

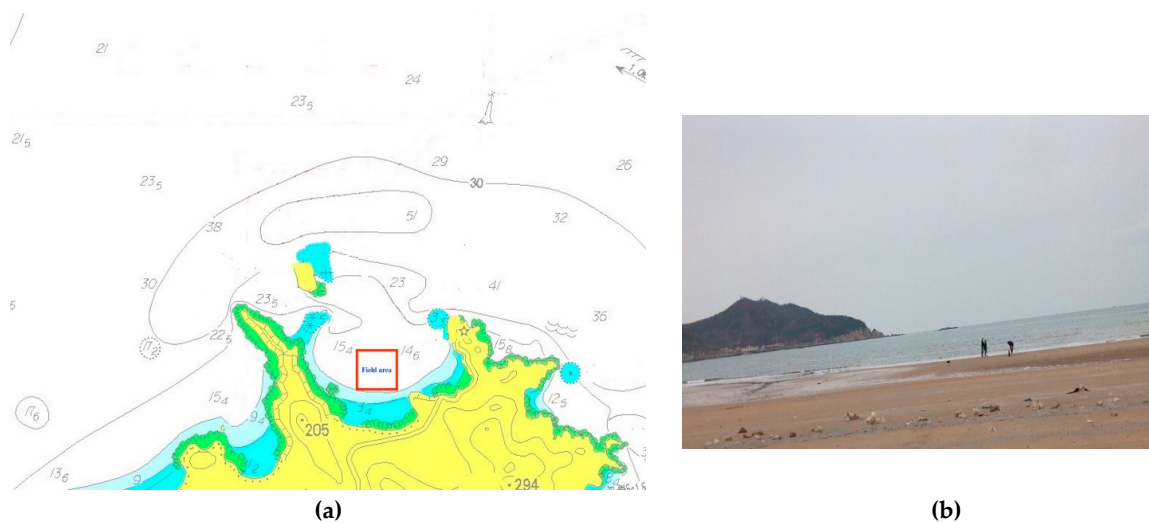


Figure 6. The experimental area. (a) The sea area of Weihai city, China. (b) The field area of the sample data.



Figure 7. Experimental equipment. (a) Beacons of a low-frequency magnetic field. (b) Magnetometer.

3.2. Optimal MLP-ANN Configuration

As shown in the above section, the number of hidden layers and the number of neurons in each hidden layer determine the complexity of the geometric structure of the MLP-ANN. While a simpler architecture of the neural network structure has a better generalization, it allows the local minima to be produced more easily. Similarly, a more complex architecture increases the ability of the neural network to avoid local minima, but it generally requires more training samples to realize a good generalization ability [79]. However, there is no empirical formula to establish the optimal architecture of MLP-ANN.

Therefore, a variety of MLP-ANN parameters were evaluated by a trial and error procedure in order to optimize the network architecture.

In the present study, we set the hyperbolic tangent activation function as the activation function; the learning algorithm is BP; the number of epochs is equal to 1000; the goal accuracy is equal to 8×10^{-4} ; and the learning rate is equal to 0.01, before optimizing the neural network. The performance of MLP-ANN was compared by changing the number of hidden layers and the number of neurons in each hidden layer. The best network architecture is selected based on several statistical criteria, including MSE and the coefficient of determination (R^2).

$$\begin{aligned} R_x^2 &= 1 - \frac{\sum_{i=1}^n [(x_i - \hat{x}_i)^2]}{\sum_{i=1}^n [(x_i - \bar{x})^2]} \\ R_y^2 &= 1 - \frac{\sum_{i=1}^n [(y_i - \hat{y}_i)^2]}{\sum_{i=1}^n [(y_i - \bar{y})^2]} \\ R_z^2 &= 1 - \frac{\sum_{i=1}^n [(z_i - \hat{z}_i)^2]}{\sum_{i=1}^n [(z_i - \bar{z}_i)^2]} \end{aligned} \quad (30)$$

where n is the number of sample data; and \bar{x} , \bar{y}_i and \bar{z}_i are average values of the sample data.

The optimal architecture of the developed ANN is shown in Figure 2. Finally, the optimal MLP ANN architecture includes two hidden layers of 40 and 20 neurons.

Figure 8 is a variation of the training error of MLP-ANN, whose architecture is optimal. It shows that the training error of MLP-ANN decreased as the number of epochs decreased. When the training procedure is at the 3950th epoch, a small tolerance is about 7.9×10^{-4} , which means that the MSE on each training data achieves the training accuracy. Therefore, the neural network is well trained.

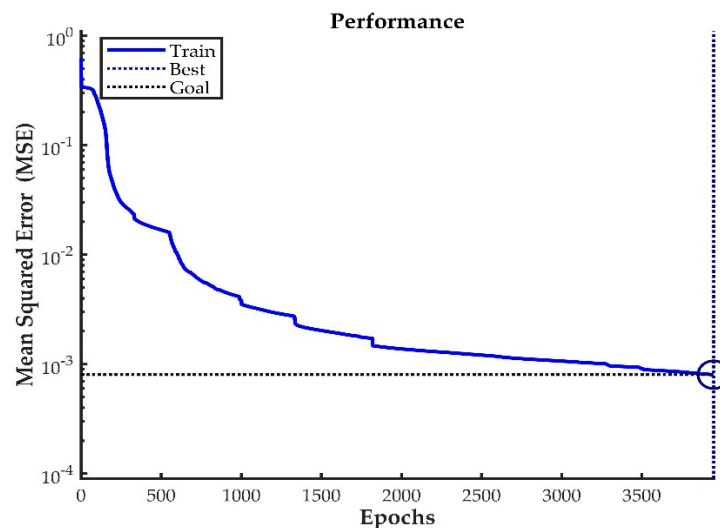


Figure 8. MLP-ANN training performance.

As stated in the previous section, 10% of the sample data were used as a test set for the optimal MLP-ANN model by trial and error. Figure 9 shows the MLP-ANN predicted values of the relative position in comparison with the true position of the sample data set. As can be seen from Figure 9, the predicted data of MLP ANN are highly consistent with the real location data.

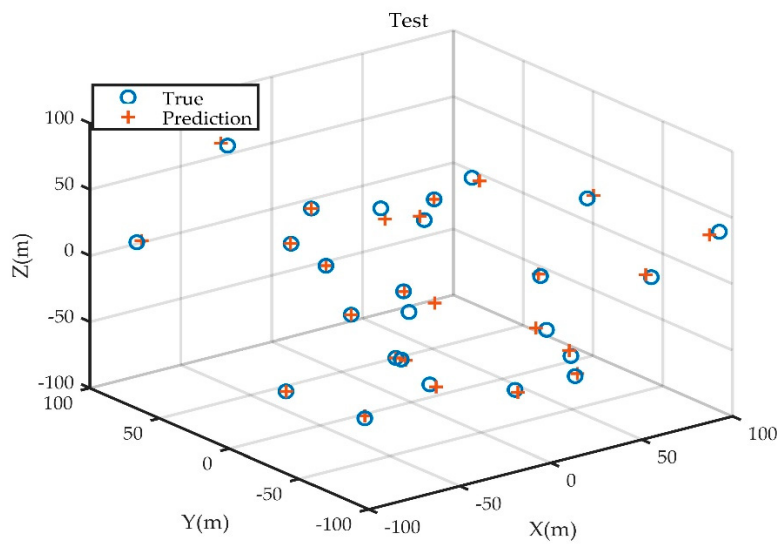


Figure 9. Comparison of the predicted relative position of the autonomous underwater vehicle (AUV) and the true position of the sample data.

Finally, in order to verify the correctness and effectiveness of the neural network method proposed in our paper, we conducted an experiment, which was a 10-fold cross-validation. We divided all samples into 10 groups (every group is composed of 100 samples) in Table 1 and adopted the cyclic approach. We selected nine groups as the training set and one group as the test set in Table 2. Each experiment was repeated 10 times, so we carried out a total of 100 experiments. Table 3 is the experimental results of cross-validation.

The division of the groups was as follows:

Table 1. Sample data number.

Team ID	Samples Number
1	1–100
2	101–200
3	201–300
4	301–400
5	401–500
6	501–600
7	601–700
8	701–800
9	801–900
10	901–1000

Table 2. Training group and testing group.

Experiment ID	Train ID	Test ID
A	1–9	10
B	1–8, 10	9
C	1–7, 9, 10	8
D	1–6, 8–10	7
E	1–5, 7–10	6
F	1–4, 6–10	5
G	1–3, 5–10	4
H	1, 2, 4–10	3
I	1, 3–10	2
J	2–10	1

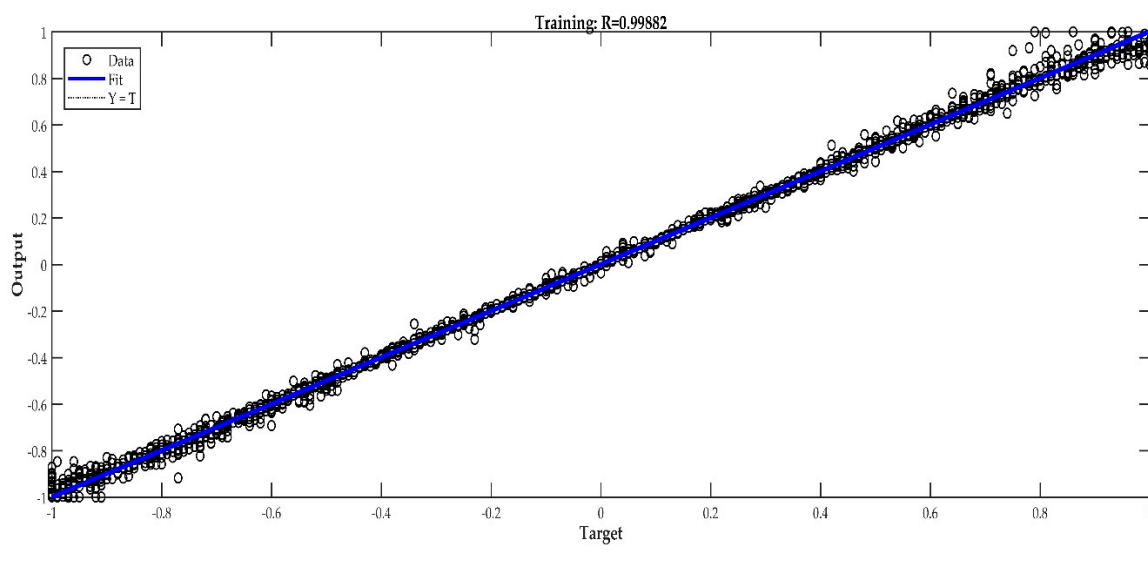
Finally, the statistical results are shown below:

Table 3. Experimental results of cross-validation.

Experiment ID	Correlation Coefficient of x Direction	Correlation Coefficient of y Direction	Correlation Coefficient of z Direction
A	0.9553	0.8368	0.9921
B	0.9234	0.8182	0.9768
C	0.9378	0.9648	0.9764
D	0.9736	0.9364	0.9242
E	0.7729	0.9372	0.9012
F	0.8251	0.8374	0.8893
G	0.9824	0.9372	0.8783
H	0.9734	0.9346	0.8940
I	0.9191	0.8237	0.9092
J	0.7732	0.6919	0.7489

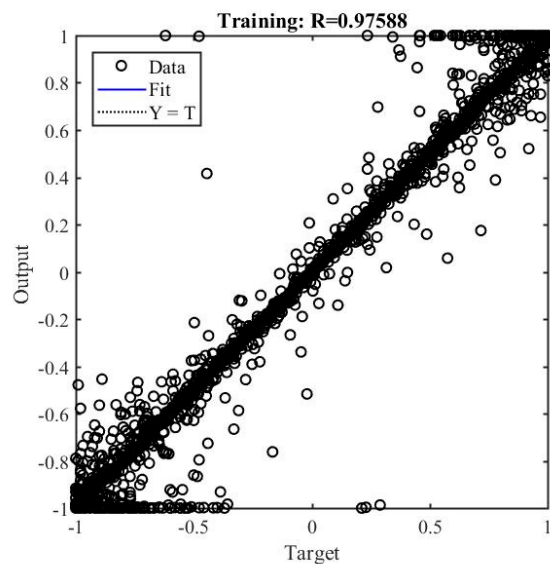
Therefore, the result of the experiment is the average result of 100 repetitions of the experiment, and the final test value of the correlation coefficient is 0.90362 in the direction of the X-axis, 0.87182 in the direction of the Y-axis, and 0.90904 in the direction of the Z-axis, which means that the ANN in our paper is effective.

As can be observed from Figure 10, all data points are scattered around the diagonal line. All the statistical analyses revealed that the proposed MLP-ANN model is a valid and accurate model for AUV position prediction.

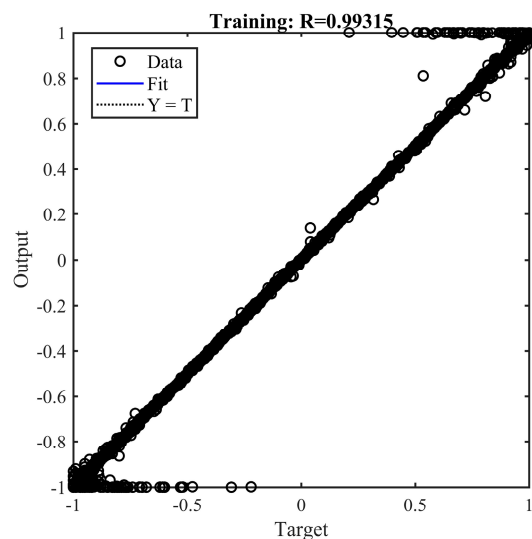


(a)

Figure 10. Cont.



(b)



(c)

Figure 10. The correlation coefficient in the X, Y, and Z-axis directions. (a) The correlation coefficient in the X-axis direction (test ID 10 in Experiment ID A). (b) The correlation coefficient in the Y-axis direction (test ID 10 in Experiment ID A). (c) The correlation coefficient in the Z-axis direction (test ID 10 in Experiment ID A).

3.3. AMB-SLAM Loop Map Simulation Setups

The following MATLAB simulation experiment is carried out for AMB-SLAM closed-loop mapping, which is performed in the context of a generic AUV observing the surrounding magnetic beacons with a range-bearing sensor in a two-dimensional area. The values of the different parameters could be changed according to the number of detected magnetic beacons and their positions in the environment, the actual speed of the robot, and the maximum observation distance of the selected sonar sensor.

The simulation environment for the AMB-SLAM closed-loop map is defined as an area of 500 m × 500 m (from 0 m to 500 m), containing 10 AUV waypoints connected in a serpentine trajectory

and 20 magnetic beacons as features distributed near the robot trajectory, as shown in Figure 11. The performance of AMB-SLAM was evaluated using the field sample data. The AUV starts off at (0 m, 0 m, 0 m), and the other essential control parameters are listed in Table 4. All the simulation experiments were implemented in MATLAB R2017a.

Table 4. Control parameters in the simulation.

Parameter	Value
Wheelbase of vehicle	2 m
Control speed input noise	3 m/s
Control heading input noise	3°
Vehicle speed	5 m/s
Observation noise	0.1 m/s
Maximum steering angle	30°
Frequency of control loops	40 Hz
Observation frequency	5 Hz
Maximum range	25 m
Maximum distance for association	8 m
Augment distance	28 m

3.4. AMB-SLAM Simulation Results and Discussion

In this study, we compared the performance of AMB-SLAM using multiple randomly distributed beacons of a low-frequency magnetic field with single fixed acoustic beacons. The estimated AUV trajectory and features achieved by AMB-SLAM are shown in Figure 11.

Figure 11 demonstrates the 2D landmark map, which was obtained using the AMB-SLAM online algorithm. The positions of the sensor scans for the point landmarks are clearly visible, and few of these sightings are rejected based on statistical outlier rejection techniques [80], since they are out of the observation range of the AUV. The rest are believed to represent landmarks and are added to the 2D map. The true landmarks are shown as blue solid stars ('★'), and the red crosses ('+') are the estimated landmark positions. The ellipses around each red cross ('+') illustrate the uncertainty covariances for the landmark coordinate estimations, and the larger they are, the more uncertain the estimated landmark horizontal positions. The estimated AUV trajectory is depicted as the solid red line, and the blue line shows the true AUV trajectory. The solid red triangle represents the acoustic beacon. A closed loop has a close relation with "positioning" and "mapping". In fact, the main meaning of the map is to inform the AUV about what is happening. At the same time, if the error is cumulative when the AUV reaches the same position, the improved algorithm loses its true meaning. As shown in Figure 11, we conducted closed-loop detection for the following scene, and the loop number here is two. In addition, we calculate the error of closed-loop detection and open-loop detection in the X and Y-axis. The error is shown in Figure 12.

Figure 11 shows that the estimated trajectory path of AMB-SLAM is much closer to the real trajectory, and the estimated magnetic beacon position of AMB-SLAM is closer to the true feature point position. Thus, the AMB-SLAM method efficiently improves the accuracy of AUV localization and the feature map. We can see from Figure 12a that the error of closed-loop detection in the X-axis is about −2 m to 2 m, while the error of open-loop detection in the X-axis is about −7 m to 3 m. From Figure 12b, it can be seen that the error of closed-loop detection in the Y-axis is about −1 m to 1 m, while the error of open-loop detection in the Y-axis is about −1 m to 7 m. The error in the estimated AUV trajectory decreases significantly when the robot completes the loop and revisits this landmark. Thus, in turn, the errors of previously detected landmark positions are reduced. Additionally, the AMB-SLAM algorithm achieves a reliable detection of cycles in the map and a consistent map update at the loop closure.

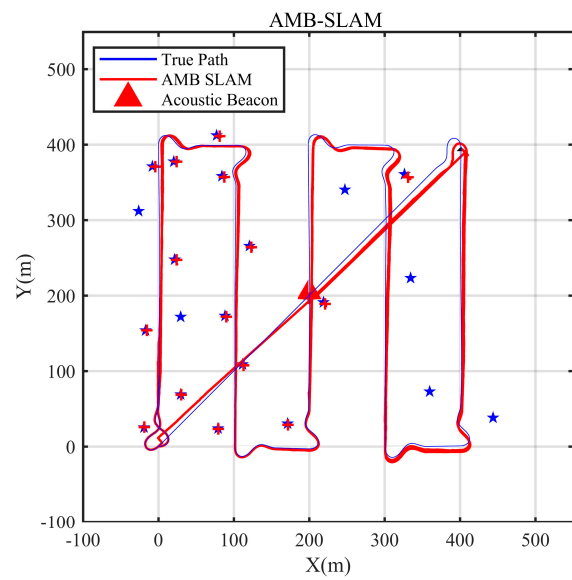
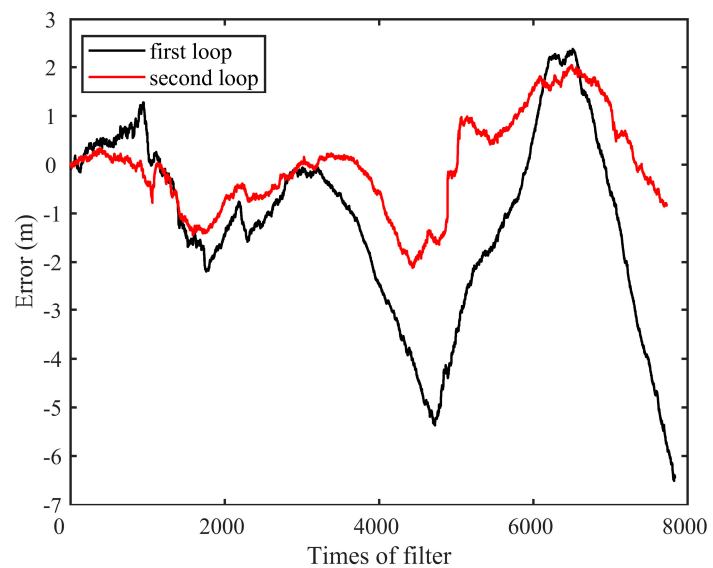
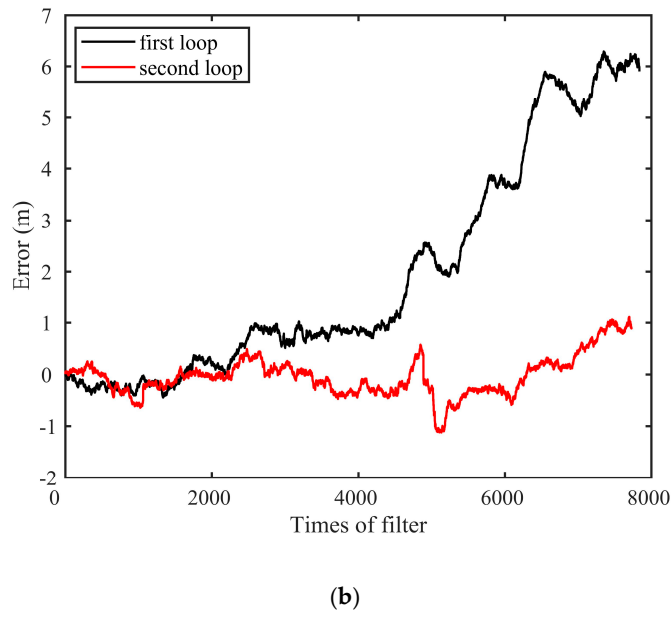


Figure 11. The AMB-SLAM closed-loop 2D map.



(a)

Figure 12. *Cont.*



(b)

Figure 12. The closed-loop and open-loop errors. (a) Comparison of the positioning error in the X-direction between the closed loop and open loop. (b) Comparison of the positioning error in the Y-direction between the closed loop and open loop.

Next, under the same simulation conditions as those tested with the AMB-SLAM method, we study the performance of the MB-SLAM algorithm, which only utilizes magnetic beacons as landmarks. Figure 13 shows the 2D trajectory map of the MB-SLAM algorithm, and Figure 14 shows the error comparison diagram of the X-axis and Y-axis of the two algorithms. We can see from Figure 14a that the error in the X-axis of MB-SLAM is about -80 m to 30 m, while the error in that of AMB-SLAM is about -2 m to 2 m. From Figure 14b, it can be seen that the error in the Y-axis of MB-SLAM is about -70 m to 0 m, while the error in that of AMB-SLAM is about -1 m to 1 m. The uncertainty in the horizontal positions of the estimated landmarks using MB-SLAM becomes bigger and bigger, and the trajectory of the AUV gradually deviates from its true position. The above phenomenon is due to the distance constraint condition of the acoustic beacon in the AMB-SLAM algorithm.

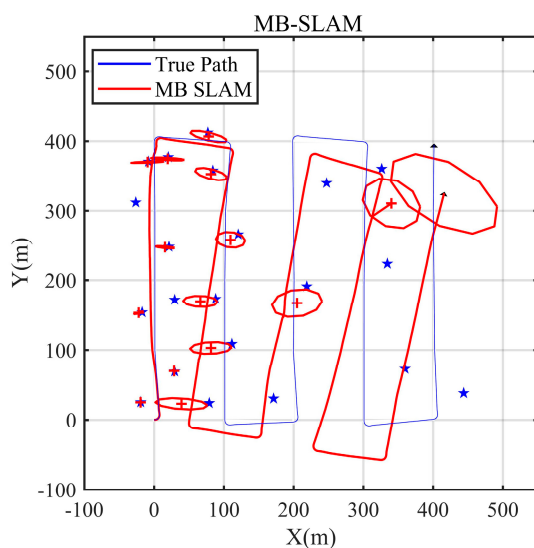


Figure 13. Positioning result using magnetic-beacon-based SLAM (MB-SLAM).

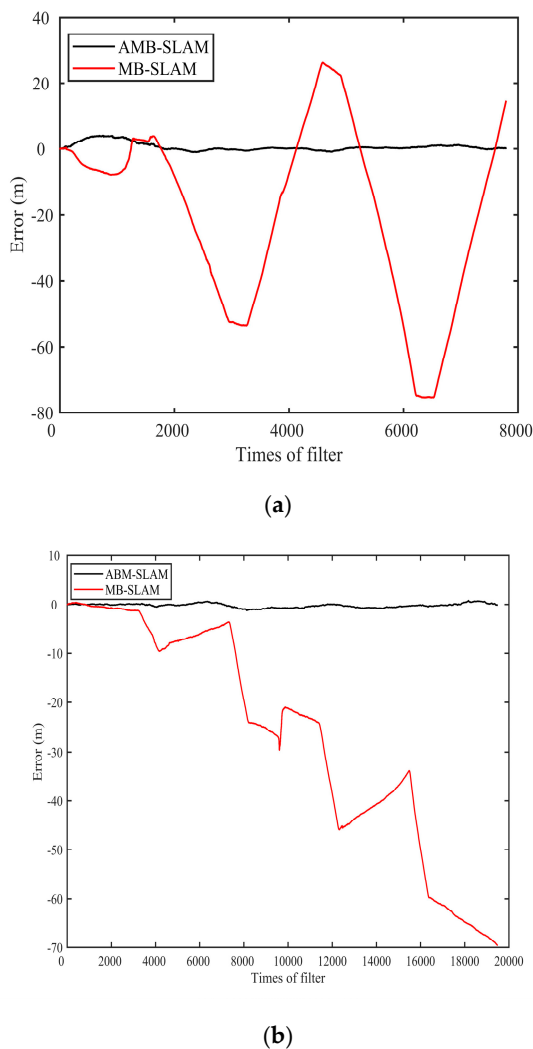
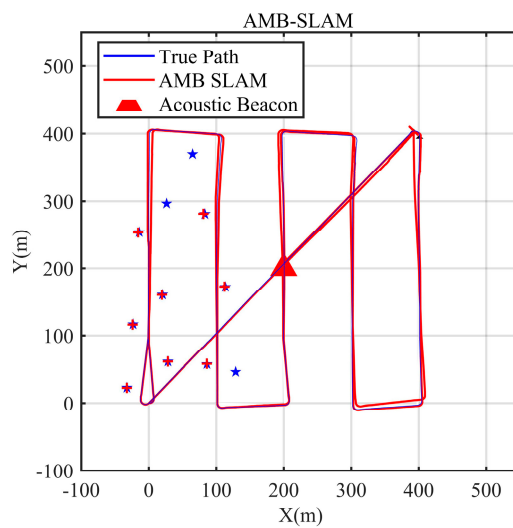
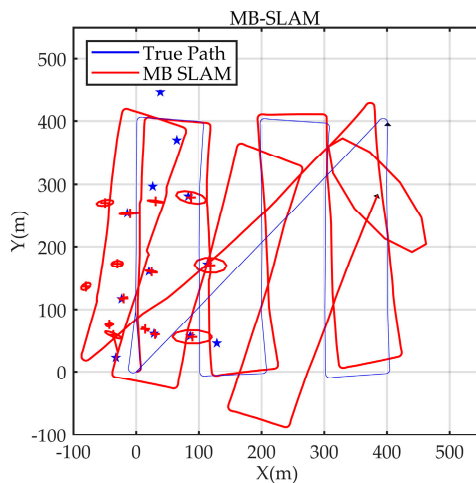
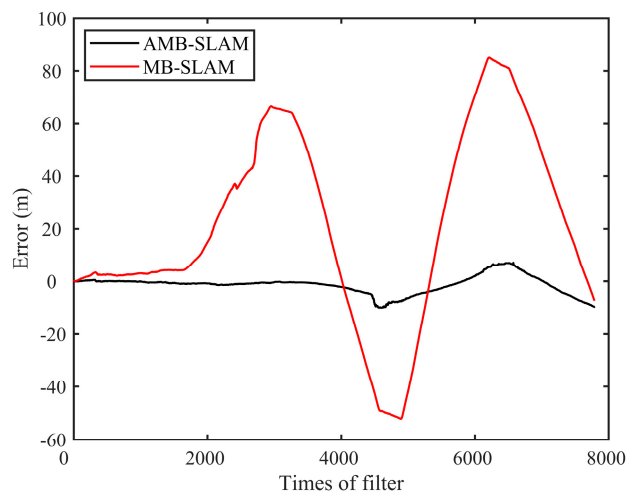


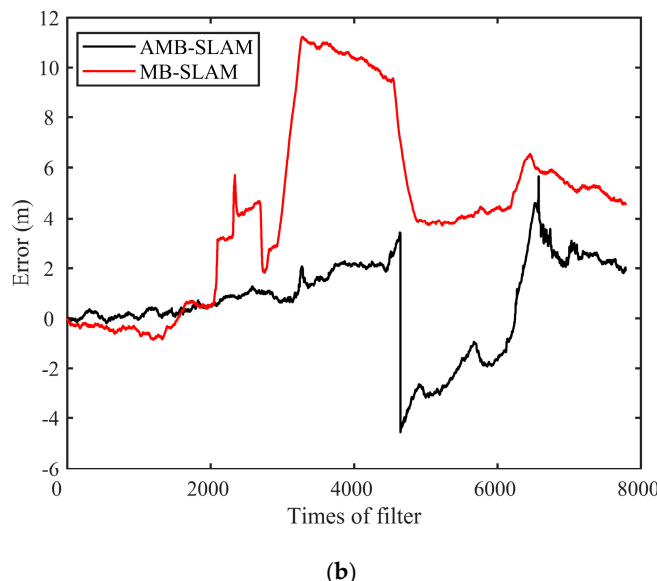
Figure 14. Comparison of the AMB-SLAM and MB-SLAM algorithms. (a) Comparison of the positioning error in the X-axis direction between AMB-SLAM and MB-SLAM. (b) Comparison of the positioning error in the Y-axis direction between AMB-SLAM and MB-SLAM.

Finally, in this study, we verified the influence of the distribution density of magnetic beacons on the performance of the AMB-SLAM and MB-SLAM algorithms. In this study, magnetic beacons are evenly distributed in the first half of the AUV path, while no magnetic beacons are distributed in the second half of the AUV planned path, which is the same as the control parameters in the previous simulation environment. The experimental results are shown in Figures 15 and 16. As can be seen from these figures, the density of the magnetic beacons has a disproportional influence on both the AMB-SLAM and MB-SLAM algorithms, but the influence on the MB-SLAM algorithm is much greater than that on MB-SLAM. In addition, we can also see from the error diagram (Figure 17) that the density of the magnetic beacons has an impact on both the AMB-SLAM and MB-SLAM algorithms, and the error in the X-axis direction of the MB-SLAM algorithm can reach -60 to 90 m. From Figure 17b, we can see that when the time is about 4200, the error in the Y-axis of the AMB-SLAM algorithm suddenly goes from 2 m to about -5 m. From this, we can draw a conclusion that the density of the magnetic beacon has an effect on both AMN-SLAM and MB-SLAM.

**Figure 15.** Positioning result using AMB-SLAM.**Figure 16.** Positioning result using MB-SLAM.

(a)

Figure 17. Cont.



(b)

Figure 17. Error diagram of the magnetic beacon density on the performance of AMB-SLAM and MB-SLAM. (a) Comparison of the positioning error on the X-axis between AMB-SLAM and MB-SLAM. (b) Comparison of the positioning error on the Y-axis between AMB-SLAM and MB-SLAM.

4. Conclusions and Future Work

4.1. Conclusions

In this study, the simultaneous localization and mapping (AMB-SLAM) algorithm for acoustic and magnetic beacons, based on MLP ANN, was proposed to allow AUVs to localize and map in a featureless seafloor environment. In our case, the 2D landmark map was chosen to represent the underwater exploring region. In order to verify the correctness and effectiveness of the neural network method in our study, the 10-fold cross-validation method was used. The results show that the presented approaches significantly improved the navigation performance of the AUV in cases where no features in the underwater field of interest are available. Firstly, the positioning accuracy of AMB-SLAM can reach approximately 1–2 m, and the positioning accuracy of the AMB-SLAM method is much higher than that of MB-SLAM. Secondly, the density of the magnetic beacons affects the positioning accuracy of AMB-SLAM and MB-SLAM. Compared with the MB-SLAM method, the AMB-SLAM algorithm has a set of redundant data regarding the relative range between the AUV and acoustic beacon, so its positioning accuracy is higher.

Compared with the existing traditional acoustic method, the INS method, the proposed method has many advantages. (1) By randomly distributing magnetic beacons, the AUV can localize and map in a featureless seafloor. (2) There is no need to deploy acoustic sensors on the seafloor and georeference them before the AUV performs its mission, as in the acoustic navigation method, which therefore allows for a low-complexity, low-cost, and high-precision solution to the AUV navigation and localization problem in featureless seawater environments. (3) The AMB-SLAM algorithm can be used for online positioning and mapping, which enables AUVs to autonomously explore or autonomously intervene in featureless seawater environments.

Compared with the existing sonar SLAM and optical SLAM algorithm, this is the first time that the SLAM method has been used to locate and map using the magnetic beacon. What is more, the computational cost of our proposed method is much lower, compared to the sonar SLAM and optical SLAM, which have to extract high-quality features from a large number of low-quality sonar or optical images. Thus, AMB-SLAM directly skips the process of extracting features as in the traditional SLAM algorithm, which allows a great deal of time to be saved and the data fusion complexity to

be reduced. Moreover, the presented AMB-SLAM algorithm has a much lower mission cost and much higher navigation precision than sonar SLAM and optical SLAM. Extracting available features is not required, as in the acoustic-based SLAM or optical-based SLAM. In conclusion, the presented AMB-SLAM method could save a lot of time and money associated with AUV missions and has a high positioning accuracy. In addition, AMB can realize real-time online positioning and mapping in featureless underwater environments.

4.2. Future Work

In the next stage of this research, in order to realize the goal of an artificially intelligent AUVs, the AMB-SLAM method that we proposed will be tested and validated with the help of the MLP ANN in the Bohai Sea, China in a featureless seawater environment, with a working area of $2000 \times 2000 \text{ m}^2$. As for further improvements to the current study, the following will be considered in future research.

(1) The proposed algorithm AMB-SLAM does have some limitations. In this study, we assume that the effect of the geomagnetic field on the magnetic field of the magnetic beacon is the same in a small area. Future research needs to prove the influence of the geomagnetic field on the magnetic beacon field in order to validate this hypothesis.

(2) In our current study, the experiments were conducted under ideal conditions. In fact, the marine environment is so complex and changeable that we need a more realistic environment to verify the stability and applicability of this method. For example, the experiments were conducted in extreme submarine environments, with a low temperature (below 0°C), high flow velocity, and high pressure ($>10 \text{ atm}$), etc.

Author Contributions: Conceptualization, Guangchao Hou and Jingsheng Zhai; methodology, Qi Shao and Guangchao Hou; software, Guangchao Hou; validation, Guangchao Hou and Liwen Dai; formal analysis, Bo Zou; investigation, Guangchao Hou, Liwen Dai, Bo Zou, Zhe Zhang, Zhehan Mu and Yadong Zhang; resources, Zhehan Mu; data curation, Yadong Zhang; writing—original draft preparation, Guangchao Hou; writing—review and editing, Guangchao Hou. All authors have read and agreed to the published version of the manuscript.

Conflicts of Interest: The authors declare no conflict of interest.

References

1. Paull, L.; Saeedi, S.; Seto, M.; Li, H. AUV Navigation and localization: A review. *IEEE J. Ocean. Eng.* **2014**, *39*, 131–149. [[CrossRef](#)]
2. Antonelli, G. *Underwater Robots*, 4th ed.; Springer: Berlin/Heidelberg, Germany, 2018; pp. 1–350.
3. Colomina, I.; Molina, P. Unmanned aerial systems for photogrammetry and remote sensing: A review. *ISPRS J. Photogramm. Remote Sens.* **2014**, *92*, 79–97. [[CrossRef](#)]
4. Tipsuwan, Y.; Hoonsuwan, P. Design and implementation of an AUV for petroleum pipeline inspection. In Proceedings of the 2015 7th International Conference on Information Technology and Electrical Engineering (ICITEE), Chiang Mai, Thailand, 29–30 October 2015; pp. 382–387.
5. Roh, H.; Joe, H.; Yu, S. Simultaneous wide area scan purpose AUV with tethered multi-agent (SWAN). In Proceedings of the 2016 IEEE/OES Autonomous Underwater Vehicles (AUV), Tokyo, Japan, 6–9 November 2016; pp. 10–13.
6. Anderson, B.; Crowell, J. Workhorse AUV-A cost-sensible new autonomous underwater vehicle for surveys/soundings, search & rescue, and research. In Proceedings of the OCEANS 2005 MTS/IEEE, Washington, DC, USA, 17–23 September 2005; pp. 1–6.
7. Matos, A.; Martins, A.; Dias, A.; Ferreira, B.; Almeida, J.M.; Ferreira, H.; Amaral, G.; Figueiredo, A.; Almeida, R.; Silva, F. Multiple robot operations for maritime search and rescue in euRathlon 2015 competition. In Proceedings of the OCEANS 2016, Shanghai, China, 10–13 April 2016; pp. 1–7.
8. Murphy, R.R.; Dreger, K.L.; Newsome, S.; Rodocker, J.; Slaughter, B.; Smith, R.; Steimle, E.; Kimura, T.; Makabe, K.; Kon, K.; et al. Marine heterogeneous multirobot systems at the great Eastern Japan Tsunami recovery. *J. Field Robot.* **2012**, *29*, 819–831. [[CrossRef](#)]

9. Yoerger, D.R.; Jakuba, M.; Bradley, A.M.; Bingham, B. Techniques for deep sea near bottom survey using an autonomous underwater vehicle. In *Springer Trac Adv Ro*, 1st ed.; Thrun, S., Brooks, R., Durrant-Whyte, H., Eds.; Springer: Berlin/Heidelberg, Germany, 2007; Volume 28, pp. 416–429.
10. Jakuba, M.V.; Roman, C.N.; Singh, H.; Murphy, C.; Kunz, C.; Willis, C.; Sato, T.; Sohn, R.A. Long-baseline acoustic navigation for under-ice autonomous underwater vehicle operations. *J. Field Robot.* **2008**, *25*, 861–879. [[CrossRef](#)]
11. Kunz, C.; Murphy, C.; Singh, H.; Pontbriand, C.; Sohn, R.A.; Singh, S.; Sato, T.; Roman, C.; Nakamura, K.-i.; Jakuba, M.; et al. Toward extraplanetary under-ice exploration: Robotic steps in the Arctic. *J. Field Robot.* **2009**, *26*, 411–429. [[CrossRef](#)]
12. Eustice, R.M.; Singh, H.; Leonard, J.J. Exactly sparse delayed-state filters for view-based SLAM. *IEEE Trans. Robot.* **2006**, *22*, 1100–1114. [[CrossRef](#)]
13. Kussat, N.H.; Chadwell, C.D.; Zimmerman, R. Absolute positioning of an autonomous underwater vehicle using GPS and acoustic measurements. *IEEE J. Ocean. Eng.* **2005**, *30*, 153–164. [[CrossRef](#)]
14. Vasilescu, I.; Detweiler, C.; Doniec, M.; Gurdan, D.; Sosnowski, S.; Stumpf, J.; Rus, D. AMOUR V: A Hovering Energy Efficient Underwater Robot Capable of Dynamic Payloads. *Int. J. Robot. Res.* **2010**, *29*, 547–570. [[CrossRef](#)]
15. LaPointe, C.E.G. Virtual Long Baseline (VLBL) Autonomous Underwater Vehicle Navigation Using a Single Transponder. Bachelor’s Thesis, Massachusetts Institute of Technology, Cambridge, MA, USA, 2006.
16. Youngberg, J.W.; Rome, N.Y. Method for Extending GPS to Underwater Applications. U.S. Patent 5119341, 2 June 1992.
17. Youngberg, J.W. A novel method for extending GPS to underwater applications. *Navigation* **1991**, *38*, 263–271. [[CrossRef](#)]
18. Sgorbini, S.; Peirano, A.; Cocito, S.; Morgigni, M. An underwater tracking system for mapping marine communities an application to Posidonia oceanica. *Oceanol. Acta* **2002**, *25*, 135–138. [[CrossRef](#)]
19. Thomas, H.G. GIB buoys an interface between space and depths of the oceans. In Proceedings of the 1998 Workshop on Autonomous Underwater Vehicles, Cambridge, MA, USA, 20–21 August 1998; pp. 181–184.
20. Alcocer, A.; Oliveira, P.; Pascoal, A. Study and implementation of an EKF GIB-based underwater positioning system. *Control Eng. Pract.* **2007**, *15*, 689–701. [[CrossRef](#)]
21. Batista, P.; Silvestre, C.; Oliveira, P. GAS tightly coupled LBL/USBL position and velocity filter for underwater vehicles. In Proceedings of the 2013 European Control Conference (ECC), Zurich, Switzerland, 17–19 July 2013; pp. 2982–2987.
22. Batista, P.; Silvestre, C.; Oliveira, P. GES integrated LBL/USBL navigation system for underwater vehicles. In Proceedings of the 51st IEEE Conference on Decision and Control, Maui, HI, USA, 10–13 December 2012; pp. 6609–6614.
23. Batista, P.; Silvestre, C.; Oliveira, P. Tightly coupled long baseline/ultra-short baseline integrated navigation system. *Int. J. Syst. Sci.* **2014**, *47*, 1837–1855. [[CrossRef](#)]
24. Vickery, K. Acoustic positioning systems. New concepts—The future. In Proceedings of the 1998 Workshop on Autonomous Underwater Vehicles, Cambridge, MA, USA, 20–21 August 1998; pp. 103–110.
25. Whitcomb, L.L.; Yoerger, D.R.; Singh, H.; Howland, J. Combined Doppler/LBL based navigation of underwater vehicles. In Proceedings of the 11th International Symposium on uNmanned Untethered Submersible Technology, Durham, NH, USA, 22–25 August 1999; pp. 1–7.
26. Spindel, R.; Porter, R.; Marquet, W.; Durham, J. A high-resolution pulse-Doppler underwater acoustic navigation system. *IEEE J. Ocean. Eng.* **1976**, *1*, 6–13. [[CrossRef](#)]
27. Panish, R.; Taylor, M. Achieving high navigation accuracy using inertial navigation systems in autonomous underwater vehicles. In Proceedings of the IEEE OCEANS 2011, Santander, Spain, 6–9 June 2011; pp. 1–7.
28. Fallon, M.F.; Kaess, M.; Johannsson, H.; Leonard, J.J. Efficient AUV navigation fusing acoustic ranging and side-scan sonar. In Proceedings of the 2011 IEEE International Conference on Robotics and Automation, Shanghai, China, 9–13 May 2011; pp. 2398–2405.
29. Morgado, M.; Oliveira, P.; Silvestre, C.; Vasconcelos, J.F. Embedded vehicle dynamics aiding for USBL/INS underwater navigation system. *IEEE Trans. Control Syst. Technol.* **2014**, *22*, 322–330. [[CrossRef](#)]
30. Watanabe, Y.; Ochi, H.; Shimura, T.; Hattori, T. Super short baseline underwater acoustic positioning supported by inertial navigation data using spread spectrum communication for autonomous underwater vehicle and error analysis in deep water. *Jpn. J. Appl. Phys.* **2009**, *48*, 1–12. [[CrossRef](#)]

31. Morgado, M.; Oliveira, P.; Silvestre, C. Tightly coupled ultrashort baseline and inertial navigation system for underwater vehicles: An experimental validation. *J. Field Robot.* **2013**, *30*, 142–170. [[CrossRef](#)]
32. Morgado, M.; Oliveira, P.; Silvestre, C.; Vasconcelos, J.F. USBL/INS tightly-coupled integration technique for underwater vehicles. In Proceedings of the 9th International Conference on Information Fusion, Florence, Italy, 10–13 July 2006; pp. 1–8.
33. Choi, W.-S.; Hoang, N.-M.; Jung, J.-H.; Lee, J.-M. Navigation system development of the underwater vehicles using the GPS/INS sensor fusion. In Proceedings of the 7th International Conference on Intelligent Robotics and Applications, Guangzhou, China, 17–20 December 2014; pp. 491–497.
34. Knight, D.T. Rapid development of tightly-coupled GPS/INS systems. *IEEE Aerosp. Electron. Syst. Mag.* **1997**, *12*, 14–18. [[CrossRef](#)]
35. Tal, A.; Klein, I.; Katz, R. Inertial Navigation System/Doppler Velocity Log (INS/DVL) fusion with partial DVL measurements. *Sensors* **2017**, *17*, 415. [[CrossRef](#)]
36. Smith, R.; Self, M.; Cheeseman, P. Estimating uncertain spatial relationships in robotics. In *Machine Intelligence and Pattern Recognition*; Lemmer, J.F., Kanal, L.N., Eds.; North-Holland: Menlo Park, CA, USA, 1988; Volume 5, pp. 435–461.
37. Smith, R.; Self, M.; Cheeseman, P. A stochastic map for uncertain spatial relationships. In Proceedings of the International Symposium on Robotics Research, Santa Clara, CA, USA, 10–11 August 1988; pp. 467–474.
38. Durrant-whyte, H.; Bailey, T. Simultaneous localization and mapping: Part I. *IEEE Robot. Autom. Mag.* **2006**, *13*, 99–108. [[CrossRef](#)]
39. Pierzchała, M.; Giguère, P.; Astrup, R. Mapping forests using an unmanned ground vehicle with 3D LiDAR and graph-SLAM. *Comput. Electron. Agric.* **2018**, *145*, 217–225. [[CrossRef](#)]
40. Kownacki, C. A concept of laser scanner designed to realize 3D obstacle avoidance for a fixed-wing UAV. *Robotica* **2014**, *34*, 243–257. [[CrossRef](#)]
41. Munguía, R.; Urzua, S.; Bolea, Y.; Grau, A. Vision-based SLAM system for unmanned aerial vehicles. *Sensors* **2016**, *16*, 372. [[CrossRef](#)] [[PubMed](#)]
42. Ma, T.; Li, Y.; Wang, R.; Cong, Z.; Gong, Y. AUV robust bathymetric simultaneous localization and mapping. *Ocean Eng.* **2018**, *166*, 336–349. [[CrossRef](#)]
43. Hidalgo, F.; Bräunl, T. Review of underwater SLAM techniques. In Proceedings of the International Conference on Automation, Robotics and Applications, Queenstown, New Zealand, 17–19 February 2015; pp. 306–311.
44. Woock, P. Survey on suitable 3D features for sonar-based underwater navigation. In Proceedings of the 2012 Oceans, Yeosu, Korea, 21–24 May 2012; pp. 1–6.
45. Eustice, R.M.; Pizarro, O.; Singh, H. Visually augmented navigation for autonomous underwater vehicles. *IEEE J. Ocean. Eng.* **2008**, *33*, 103–122. [[CrossRef](#)]
46. Eustice, R.M.; Singh, H.; Leonard, J.J.; Walter, M.R. Visually mapping the RMS titanic: Conservative covariance estimates for SLAM information filters. *Int. J. Robot. Res.* **2006**, *25*, 1223–1242. [[CrossRef](#)]
47. Fairfield, N.; Kantor, G.; Jonak, D.; Wettergreen, D. Autonomous exploration and mapping of flooded sinkholes. *Int. J. Robot. Res.* **2010**, *29*, 748–774. [[CrossRef](#)]
48. Fairfield, N.; Kantor, G.; Wettergreen, D. Real-time SLAM with Octree evidence grids for exploration in underwater tunnels. *J. Field Robot.* **2007**, *24*, 3–21. [[CrossRef](#)]
49. Maki, T.; Kondo, H.; Ura, T.; Sakamaki, T. Imaging vent fields: SLAM based navigation scheme for an AUV toward large-area seafloor imaging. In Proceedings of the 2008 IEEE/OES Autonomous Underwater Vehicles, Woods Hole, MA, USA, 13–14 October 2008; pp. 1–10.
50. Barkby, S.; Williams, S.B.; Pizarro, O.; Jakuba, M.V. Bathymetric particle filter SLAM using trajectory maps. *Int. J. Robot. Res.* **2012**, *31*, 1409–1430. [[CrossRef](#)]
51. Barkby, S.; Williams, S.B.; Pizarro, O.; Jakuba, M.V. A featureless approach to efficient bathymetric SLAM using distributed particle mapping. *J. Field Robot.* **2011**, *28*, 19–39. [[CrossRef](#)]
52. Barkby, S.; Williams, S.; Pizarro, O.; Jakuba, M. An efficient approach to bathymetric SLAM. In Proceedings of the 2009 IEEE/RSJ International Conference on Intelligent Robots and Systems, St. Louis, MO, USA, 11–15 October 2009; pp. 219–224.
53. Roman, C.; Singh, H. Improved vehicle based multibeam bathymetry using sub-maps and SLAM. In Proceedings of the 2005 IEEE/RSJ International Conference on Intelligent Robots and Systems, Edmonton, AB, Canada, 2–6 August 2005; pp. 3662–3669.

54. Zandara, S.; Ridao, P.; Mallios, A.; Ribas, D. MBpIC-SLAM: Probabilistic surface matching for bathymetry based SLAM. *IFAC Proc. Vol.* **2012**, *45*, 126–131. [[CrossRef](#)]
55. Ruiz, I.T.; Raucourt, S.d.; Petillot, Y.; Lane, D.M. Concurrent mapping and localization using sidescan sonar. *IEEE J. Ocean. Eng.* **2004**, *29*, 442–456. [[CrossRef](#)]
56. Jaulin, L. A nonlinear set membership approach for the localization and map building of underwater robots. *IEEE Trans. Robot.* **2009**, *25*, 88–98. [[CrossRef](#)]
57. Woock, P.; Frey, C. Deep-sea AUV navigation using side-scan sonar images and SLAM. In Proceedings of the OCEANS’10 IEEE SYDNEY, Sydney, Australia, 24–27 May 2010; pp. 1–8.
58. Aulinas, J.; Lladó, X.; Salvi, J.; Petillot, Y.R. Feature based slam using side-scan salient objects. In Proceedings of the OCEANS 2010 MTS/IEEE SEATTLE, Seattle, WA, USA, 20–23 September 2010; pp. 1–8.
59. Walter, M.; Hover, F.; Leonard, J. SLAM for ship hull inspection using exactly sparse extended information filters. In Proceedings of the 2008 IEEE International Conference on Robotics and Automation, Pasadena, CA, USA, 19–23 May 2008; pp. 1463–1470.
60. Shippey, G.; Jonsson, M.; Pihl, J.N.B. Position correction using echoes from a navigation fix for synthetic aperture sonar imaging. *IEEE J. Ocean. Eng.* **2009**, *34*, 294–306. [[CrossRef](#)]
61. Newman, P.M.; Leonard, J.J.; Rikoski, R.J. Towards constant-time SLAM on an autonomous underwater vehicle using synthetic aperture sonar. In *Proceedings of the 11th International Symposium of Robotics Research*; Springer: Berlin/Heidelberg, Germany, 2005; pp. 409–420.
62. Ribas, D.; Ridao, P.; Tardós, J.D.; Neira, J. Underwater SLAM in man-made structured environments. *J. Field Robot.* **2008**, *25*, 898–921. [[CrossRef](#)]
63. Ribas, D.; Ridao, P.; Neira, J.; Tardós, J.D. SLAM using an imaging sonar for partially structured underwater environments. In Proceedings of the 2006 IEEE/RSJ International Conference on Intelligent Robots and Systems, Beijing, China, 9–15 October 2006; pp. 5040–5045.
64. Mallios, A.; Ridao, P.; Hernandez, E.; Ribas, D.; Maurelli, F.; Petillot, Y. Pose-based SLAM with probabilistic scan matching algorithm using a mechanical scanned imaging sonar. In Proceedings of the OCEANS 2009-EUROPE, Bremen, Germany, 11–14 May 2009; pp. 1–6.
65. Ferreira, F.; Veruggio, G.; Caccia, M.; Bruzzone, G. Real-time optical SLAM-based mosaicking for unmanned underwater vehicles. *Intell. Serv. Robot.* **2012**, *5*, 55–71. [[CrossRef](#)]
66. Bleser, G.; Hendeby, G. Using optical flow as lightweight SLAM alternative. In Proceedings of the 2009 8th IEEE International Symposium on Mixed and Augmented Reality, Orlando, FL, USA, 19–22 October 2009; pp. 175–176.
67. Wang, P.; Chen, C.; Dong, C.; Xu, H.; Tian, F. The analysis method of video camera’s motion based on optical flow and slam. In Proceedings of the 2016 International Conference on Audio, Language and Image Processing (ICALIP), Shanghai, China, 11–12 July 2016; pp. 62–66.
68. Andert, F.; Ammann, N.; Krause, S.; Lorenz, S.; Bratanov, D.; Mejias, L. Optical-aided aircraft navigation using decoupled visual SLAM with range sensor augmentation. *J. Intell. Robot. Syst.* **2017**, *88*, 547–565. [[CrossRef](#)]
69. Neira, J.; Tardós, J.D. Data association in stochastic mapping using the joint compatibility test. *IEEE Trans. Robot. Autom.* **2001**, *17*, 890–897. [[CrossRef](#)]
70. Davis, C. GPS-like navigation underground. In Proceedings of the IEEE/ION Position, Location and Navigation Symposium, Indian Wells, CA, USA, 4–6 May 2010; pp. 1108–1111.
71. Shanmuganathan, S. Artificial neural network modelling: An introduction. In *Artificial Neural Network Modelling*; Springer: Berlin/Heidelberg, Germany, 2016; pp. 1–14.
72. Masters, T. *Practical Neural Network Recipes in C++*, 1st ed.; Academic Press: Cambridge, MA, USA, 1993; pp. 1–493.
73. Burden, F.R.; Brereton, R.G.; Walsh, P.T. Cross-validatory selection of test and validation sets in multivariate calibration and neural networks as applied to spectroscopy. *Analyst* **1997**, *122*, 1015–1022. [[CrossRef](#)]
74. Minns, A.W.; Hall, M.J. Artificial neural networks as rainfall-runoff models. *Hydrol. Sci. J. Sci. Hydrol.* **1996**, *41*, 399–417. [[CrossRef](#)]
75. White, H. Learning in artificial neural networks: A statistical perspective. *Neural Comput.* **1989**, *1*, 425–464. [[CrossRef](#)]
76. Parisi, R.; Claudio, E.D.D.; Orlandi, G.; Rao, B.D. A generalized learning paradigm exploiting the structure of feedforward neural networks. *IEEE Trans. Neural Netw.* **1996**, *7*, 1450–1460. [[CrossRef](#)] [[PubMed](#)]

77. Amari, S.; Murata, N.; Muller, K.; Finke, M.; Yang, H.H. Asymptotic statistical theory of overtraining and cross-validation. *IEEE Trans. Neural Netw.* **1997**, *8*, 985–996. [[CrossRef](#)] [[PubMed](#)]
78. Maier, H.R.; Dandy, G.C. Neural networks for the prediction and forecasting of water resources variables: A review of modelling issues and applications. *Environ. Modell. Softw.* **2000**, *15*, 101–124. [[CrossRef](#)]
79. Bebis, G.; Georgopoulos, M. Feed-forward neural networks. *IEEE Potentials* **1994**, *13*, 27–31. [[CrossRef](#)]
80. Dissanayake, M.W.M.G.; Newman, P.; Clark, S.; Durrant-Whyte, H.F.; Csorba, M. A solution to the simultaneous localization and map building (SLAM) problem. *IEEE Trans. Robot. Autom.* **2001**, *17*, 229–241. [[CrossRef](#)]



© 2019 by the authors. Licensee MDPI, Basel, Switzerland. This article is an open access article distributed under the terms and conditions of the Creative Commons Attribution (CC BY) license (<http://creativecommons.org/licenses/by/4.0/>).